Article

Fast Li⁺ Transfer Scaffold Enables Stable High-Rate All-Solid-State Li Metal Batteries

Libo Song [1,2], Yuanyue He [1,2], Zhendong Li [2] (ID), Zhe Peng [2,3,*] (ID) and Xiayin Yao [2,3,*]

1   School of Materials Science and Chemical Engineering, Ningbo University, Ningbo 315211, China
2   Ningbo Institute of Materials Technology and Engineering, Chinese Academy of Sciences,
    Ningbo 315201, China
3   Center of Materials Science and Optoelectronics Engineering, University of Chinese Academy of Sciences,
    Beijing 100049, China
*   Correspondence: pengzhe@nimte.ac.cn (Z.P.); yaoxy@nimte.ac.cn (X.Y.)

Abstract: Sluggish transfer kinetics caused by solid–solid contact at the lithium (Li)/solid-state electrolyte (SE) interface is an inherent drawback of all-solid-state Li metal batteries (ASSLMBs) that not only limits the cell power density but also induces uneven Li deposition as well as high levels of interfacial stress that deteriorates the internal structure and cycling stability of ASSLMBs. Herein, a fast Li⁺ transfer scaffold is proposed to overcome the sluggish kinetics at the Li/SE interface in ASSLMBs using an α-MnO$_2$-decorated carbon paper (CP) structure (α-MnO$_2$@CP). At an atomic scale, the tunnel structure of α-MnO$_2$ exhibits a great ability to facilitate Li⁺ adsorption and transportation across the inter-structure of α-MnO$_2$@CP, leading to a high critical current density of 3.95 mA cm^{-2} at the Li/SE interface. Meanwhile, uniform Li deposition can be guided along the skeletons of α-MnO$_2$@CP with minimized volume expansion, significantly improving the structural stability of the Li/SE interface. Based on these advantages, the ASSLMBs using α-MnO$_2$@CP protected the Li anode and can stably cycle up to very high charge/discharge rates of 10C/10C, paving the way for developing high-power ASSLMBs.

Keywords: all-solid-state Li metal battery; Li metal anode; solid electrolyte; dendrite; Li⁺ transfer kinetics

1. Introduction

Lithium (Li)-ion batteries (LIB) are widely used in portable devices and electric vehicles [1,2]. However, due to the use of low-capacity graphite anodes, the energy density of LIBs is insufficient to support the surging increase in battery endurance requirements [3]. To improve the energy density of rechargeable Li-based batteries, replacing graphite with a Li metal with a low redox potential (−3.04 V vs. standard hydrogen electrode) and a high theoretical specific capacity (3860 mAh g^{-1}) is a rational option [4]. However, the use of a Li metal anode is associated with serious safety concerns due to uncontrolled dendrite growth that can pierce the separator and eventually cause thermal runaway and a fire or an explosion of the batteries using highly flammable organic liquid electrolytes [5]. All-solid-state Li metal batteries (ASSLMBs) that use nonflammable solid-state electrolytes (SEs) are a promising approach to overcome the safety issue caused by Li metal anodes [6]. However, retaining a stable interface between the Li metal and the SE for long-term cycling is challenged due to the serious dendrite growth and side reactions that cause fast SE cracks and decompositions followed by radical performance fading [7].

To stabilize the Li/SE interface, building functional artificial layers is the main option that has been proposed. Using a Li⁺ conducting interlayer, such as glass fibers supported by a LiTFSI/LiNO$_3$ film [8], a chemically vapor-deposited Li$_2$Se layer [9], and a solvent–LiTFSI complex layer [10,11], efficient separation between the Li metal anode and the SE

can be achieved to suppress the interfacial side reactions, and a more fluent Li^+ transportation can also be enabled by the artificial layers, resulting in improved cyclic stability of ASSLMBs. Li alloy-based interlayers with high Li affinity were also applied as one class of efficient dendrite inhibitors between Li and SE, where Mg- [12], Zn- [13], Ag- [14,15], and Si-based [16] interlayers were separately demonstrated to be promising candidates to sustainably suppress dendrite growth for long-term cycling of ASSLMBs.

Despite the significant progress in Li protection, the sluggish transfer kinetics involved in the solid–solid contact at the Li/SE interface still remains a critical issue hindering the practical requirements of ASSLMBs, and novel approaches adapted to accelerate the interfacial Li^+ transfer in ASSLMBs have yet to be established. Herein, an α-MnO_2 possessing a large tunnel structure that facilitates rapid Li^+ diffusion was coated on three-dimensional carbon paper (CP) to fabricate a fast Li^+ transfer scaffold (α-MnO_2@CP) [17,18], with the aim of overcoming the sluggish kinetics at the Li/SE interface in ASSLMBs. It was revealed that the tunnel structure of α-MnO_2 endowed α-MnO_2@CP with facilitated Li^+ adsorption and transportation across the inter-structure, resulting in a high critical current density of 3.95 mA cm^{-2} at the Li/SE interface. Based on the accelerated Li^+ transport, Li deposition on α-MnO_2@CP also featured high uniformity along the skeletons of the scaffold, significantly improving the structural stability of the Li/SE interface. Consequently, the ASSLMBs using α-MnO_2@CP protected the Li anode and enabled stable cycling up to very high charge/discharge rates of 10C/10C, demonstrating the potential to construct high-power ASSLMBs via a Li/SE interfacial Li^+ transfer boost.

2. Experimental Section

2.1. Material Preparations

To prepare α-MnO_2@CP, 0.735 g $Mn(CH_3COO)_2 \cdot 4H_2O$ (Aladdin, Shanghai, China) was dissolved in a solution consisting of 20 mL deionized water and 10 mL absolute ethanol followed by stirring at 60 °C for 1 h. Then, 0.3175 g $KMnO_4$ (Aladdin, Shanghai, China) was added to the solution followed by stirring for 30 min. Several pieces of CP (Carbon Paper, Toray Industries, Inc., Tokyo, Japan) were added to the above solution, and the solution was transferred to a 100 mL autoclave with a Teflon liner where it was maintained at 120 °C for 12 h. After cooling down to room temperature, the products were washed with deionized water/ethanol three times and freeze-dried in a vacuum for 12 h to obtain α-MnO_2@CP.

2.2. Material Characterizations

Scanning electron microscope (SEM) and energy dispersive spectroscope (EDS) images were recorded using a QUANTA FEG 250, FEI (Hilsboro, OR, USA). The optical images were recorded using a Leica DVM6 microscope (Wetzlar, Germany). The crystalline phases were detected by X-ray diffraction (XRD) with a Bruker D8 advanced diffractometer using Cu K_α (λ = 1.5406 Å) radiation (Bruker AXS, D8 Advance DaVinci, Karlsruhe, Germany). An X-ray photoelectron spectrometer (XPS, Kratos, Axis Ultra DLD, Manchester, UK) was excited by a Mg K_α radiation source at a constant power of 100 W (15 kV and 6.67 mA). Brunauer–Emmett–Teller (BET) measurements were performed using a Micromeritics ASAP 2020HD88 (Norcross, GA, USA).

2.3. Electrochemical Measurements

All the battery assemblies were carried out in an argon-filled glove box. Lithium hexafluorophosphate ($LiPF_6$), ethylene carbonate (EC), diethyl carbonate (DEC), and fluoroethylene carbonate (FEC) were purchased from Aladdin. The routine electrolyte used in this work was 1 M $LiPF_6$ in EC:DEC:FEC (1:1:1 by volume). Li‖Li symmetrical cells were assembled by placing two identical carbon interlayers at each side of the separator, and the carbon interlayer/separator/carbon interlayer structure was sandwiched between two Li foils. Cyclic voltammetry (CV) tests were performed on Li‖Li cells at various scan rates from 4 to 12 mV s^{-1} with an increment of 2 mV s^{-1} in a voltage window between −15 and

15 mV. Electrochemical impedance spectroscopy (EIS) measurements were performed on the Li || α-MnO$_2$@CP half cell, in which α-MnO$_2$@CP was used as the working electrode, and Li foil was used as the counter and reference electrodes. The EIS spectra were recorded in a frequency range from 10^6 to 10^{-1} Hz with a voltage perturbation of 10 mV. The CV and EIS measurements were carried out using a potentionstat/galvanostat (1470E) equipped with a frequency response analyzer (1455A) from Solartron.

To assemble the all-solid-state Li || Li symmetrical cells, a pellet with a 10 mm diameter was prepared by pressing a 150 mg Li$_6$PS$_5$Cl solid electrolyte at 180 MPa in a polytetrafluoroethylene mold. Two identical carbon interlayers were placed on each side of the electrolyte pellet and pressed at 360 MPa, followed by the placement of two Li foils on each side of the carbon interlayer/electrolyte/carbon interlayer composite and pressing at 90 MPa. Critical current density (CCD) measurements were carried out using the all-solid-state Li || Li symmetrical cells. The CCD tests started with a current density of 0.05 mA cm^{-2}, followed by a stepwise current increase of 0.05 mA cm^{-2} until the cell short circuited. The CV tests of the all-solid-state Li || Li symmetrical cells were performed at a scan rate of 0.5 mV s^{-1} in a voltage window between -10 and 10 mV. To assemble the ASSLMBs, LiNbO$_3$-coated LiCoO$_2$ powders and a Li$_6$PS$_5$Cl electrolyte were mixed at a weight ratio of 7:3 and then uniformly spread on the electrolyte pellet and pressed under 240 MPa to form a composite cathode. Finally, the CP or α-MnO$_2$@CP interlayer was placed on the other side of the electrolyte pellet followed by the attachment of a Li foil and pressing at 360 MPa. The mass loading of the LiCoO$_2$ cathode in this work was ~1.8 mg cm^{-2}, and the current density corresponding to the 1C rate was ~0.22 mA cm^{-2}. The Li foil used for the all-solid-state battery assembly had a thickness of 80 μm. The all-solid-state full cells were cycled at selected charge/discharge rates in a voltage window of 3.0–4.2 V.

3. Results and Discussion

XRD patterns of α-MnO$_2$@CP and scrapped α-MnO$_2$ powders from α-MnO$_2$@CP are shown in Figure 1a, where the characteristic peaks of α-MnO$_2$ are well identified, demonstrating the successful coating of the α-MnO$_2$ shell on the CP matrix. The successful α-MnO$_2$ coating on the CP was also demonstrated by the Raman spectrum of α-MnO$_2$@CP, where the characteristic Raman peaks corresponding to α-MnO$_2$ (below 900 cm^{-1}) are clearly observed (Figure 1b) [19]. The crystal structure of α-MnO$_2$ contains 2×2 edge shared MnO$_6$ octahedral units [17,18], where the large tunnel structure endows α-MnO$_2$ with a noticeable ability to accommodate various cations with different sizes, such as Li and Mg [20,21]. Herein, the large tunnel structure of α-MnO$_2$ is expected to provide channels that allow for the speedy diffusion of Li$^+$ across the interconnected skeletons of α-MnO$_2$@CP, which together result in a high Li$^+$ flux interlayer between Li and SE. The morphology of α-MnO$_2$@CP was studied by SEM and EDS images. Compared with bare CP (Figure S1), uniform coverage of the fibrous α-MnO$_2$ shell was clearly observed on α-MnO$_2$@CP (Figure 1c). The cross-sectional SEM and EDS images of α-MnO$_2$@CP further demonstrate the core–shell structure with a CP core and an α-MnO$_2$ shell (Figure S2). Meanwhile the BET measurement of α-MnO$_2$@CP showed a surface area of 5.6246 m^2 g^{-1} (Figure S3). The well-developed α-MnO$_2$ shell is expected to provide continuous high-speed Li$^+$ migration paths throughout the whole scaffold structure.

In a Li$^+$ mobility-limited environment such as ASSLMBs, the efficient capture (or adsorption) of Li$^+$ is particularly important for the artificial Li protective structure since it can, in turn, promote the fluency of Li$^+$ transport at the Li/SE interface. Meanwhile, the great ability of Li$^+$ regarding electrochemical capture is a particular advantage of α-MnO$_2$, enabling it to have wide-ranging applications in Li-ion battery electrodes [21], Li-based supercapacitors [22], and Li–air battery catalysts [23]. Hence, the effect of the α-MnO$_2$ shell on the ability of α-MnO$_2$@CP to adsorb Li$^+$ was studied by assessing the double-layer capacitance of Li || Li symmetrical cells using a liquid electrolyte with CP or α-MnO$_2$@CP interlayers. CV curves were recorded by cycling the Li || Li symmetrical cells at different scan rates (Figure 2a,b), where the curves of the cell using α-MnO$_2$@CP

(Figure 2b) clearly exhibited an additional capacitive feature compared with those of the cell using CP (Figure 2a). By further plotting the mean response current density as a function of scan rate, the double-layer capacitances were determined (Figure 2c), and the double-layer capacitance of the cell using α-MnO$_2$@CP (10.49 mF cm^{-2}) was about 50 times higher than that of the cell using CP (0.21 mF cm^{-2}). These results demonstrate the strong Li$^+$ adsorption ability of the α-MnO$_2$ shell, which is of great importance in boosting the Li$^+$ transfer kinetics at the Li/SE interface via the introduction of the α-MnO$_2$@CP interlayer. The latter was demonstrated by the CV measurements carried out in all-solid-state Li||Li symmetrical cells. As shown in Figure S4, in a voltage window between -10 and 10 mV, the higher response current density of the cell using the α-MnO$_2$@CP interlayer compared with the cell using CP indicates a better charge and better mass transfer kinetics at the Li/SE interface, which is enabled by the speedy Li$^+$ transportation in the α-MnO$_2$ channels.
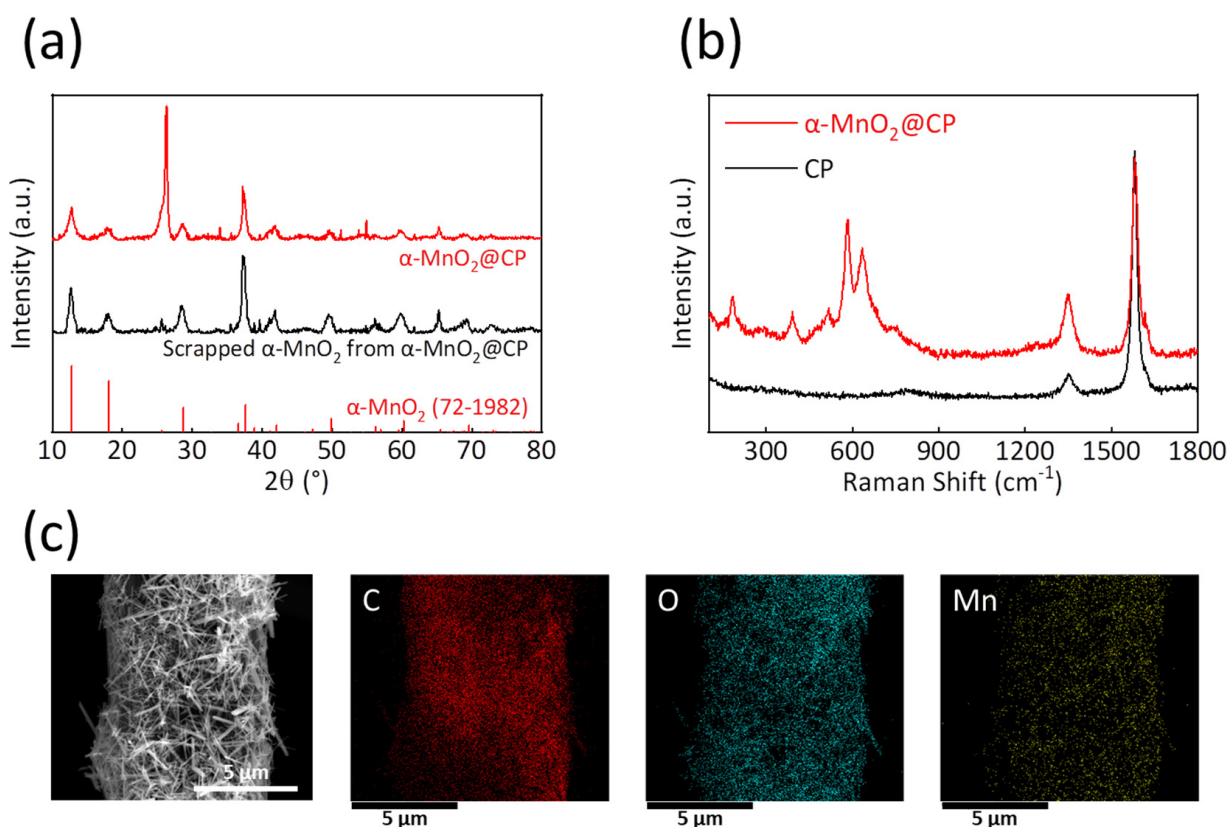

Figure 1. (**a**) XRD pattern of α-MnO$_2$@CP and scrapped α-MnO$_2$ powders from α-MnO$_2$@CP. (**b**) Raman spectrum of CP and α-MnO$_2$@CP. (**c**) SEM and EDS images of α-MnO$_2$@CP.

To further study the ability of α-MnO$_2$@CP to enhance the Li$^+$ transfer kinetics at the Li/SE interface, CCD was assessed using all-solid-state Li||Li symmetrical cells. As shown in Figure 2d, a high CCD of 3.95 mA cm^{-2} was achieved for the cell using α-MnO$_2$@CP, while the CCD value for the cell without an artificial interlayer was only 0.2 mA cm^{-2} (Figure S5a). It is noteworthy that the high CCD enabled by α-MnO$_2$@CP mainly resulted from the α-MnO$_2$ shell, since the only use of CP was not able to raise the CCD significantly (Figure S5b). This result also indicates the insufficiency of 3D current collectors to improve the Li$^+$ transfer kinetics in ASSLMBs despite their great effect of improving the cycling stability of Li metal anode in the batteries using liquid electrolytes [24,25]. In the Li metal batteries using liquid electrolytes, the deep permeation of electrolyte in the pore space of 3D current collectors can lead to the formation of a highly cross-linked solid electrolyte interface (SEI) matrix that conducts Li$^+$ across the entire structure. However, this structural transition cannot be achieved in ASSLMBs due to the limited contact surface area at the Li/SE interface. Hence, building an efficient Li$^+$-conducting medium should be a priority

for the design of a Li-protective structure in ASSLMBs, and the α-MnO$_2$ shell is herein demonstrated to be a rational choice. It should be noted that a comparison of CCD between the results of this work and those from the recent literature has been made (Table S1), further reflecting the good interfacial transfer kinetics enabled by α-MnO$_2$@CP compared with other reported methods.
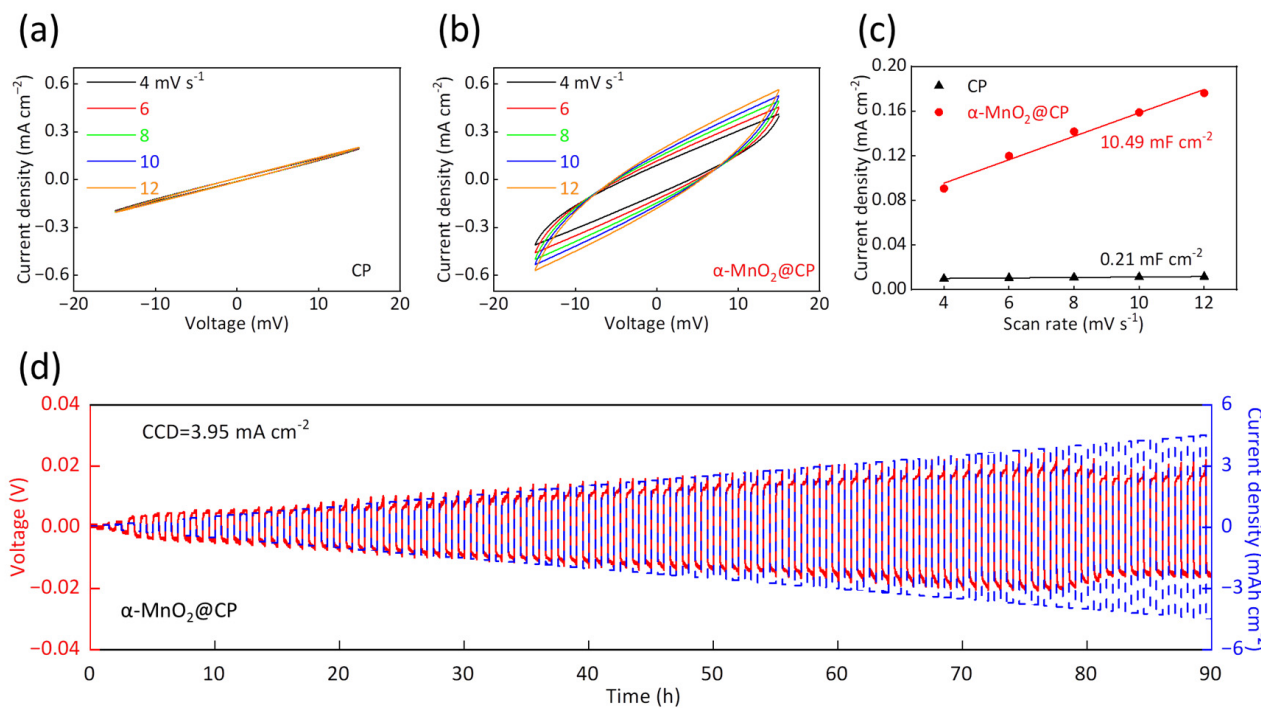

Figure 2. CV curves of Li||Li symmetrical cells using (**a**) CP or (**b**) α-MnO$_2$@CP interlayers at different scan rates. (**c**) Double-layer capacitance determination for CP and α-MnO$_2$@CP interlayers. These CV measurements were performed within Li||Li symmetrical cells using liquid electrolyte. (**d**) Voltage profile of CCD measurement for all-solid-state Li||Li symmetrical cell using α-MnO$_2$@CP interlayer between Li and SE.

Based on the above results, a comprehensive understanding of the improved Li$^+$ transfer dynamics enabled by α-MnO$_2$@CP is needed. As the lithiation state and crystal structure of α-MnO$_2$ are strongly coupled [17], which can, in turn, affect the Li$^+$ transportation in the tunnel structure of α-MnO$_2$, the relationship between the lithiation state and Li$^+$ conducting ability of α-MnO$_2$@CP should be an important issue. Since the lithiation of α-MnO$_2$ is accompanied by a Mn valence state change, XPS was employed to probe the valence states of Mn in the α-MnO$_2$ shell of α-MnO$_2$@CP at different states during the lithiation/delithiation processes, which has been pointed out on the discharge/charge curve of α-MnO$_2$@CP in Figure 3a. At state 1 before cycling, only Mn^{4+} signals were observed (Figure 3b), corresponding to the valence state of pristine α-MnO$_2$. As discharge proceeded (state 2, Figure 3a), signals related to lower Mn valence states (2+ and 3+) were clearly observed on the Mn 2p spectrum of α-MnO$_2$@CP (Figure 3c), reflecting the reduction of Mn ions by the Li insertion in the tunnel structure. When a full lithiation state was achieved at 0 V (state 3, Figure 3a), the peak area ratio corresponding to Mn^{4+} consistently decreased to a minimum (Figure 3d). It is noteworthy that a valence state reversibility of Mn was observed upon charging (delithiation process), as shown by the restored peak intensity of Mn^{4+} at state 4 (Figure 3e). Furthermore, the peaks of Mn^{2+} and Mn^{3+} remained even when the half cell was charged up to 3 V (Figure 3f), indicating one part of the irreversible α-Li$_x$MnO$_2$ phases on α-MnO$_2$@CP after the initial cycling.
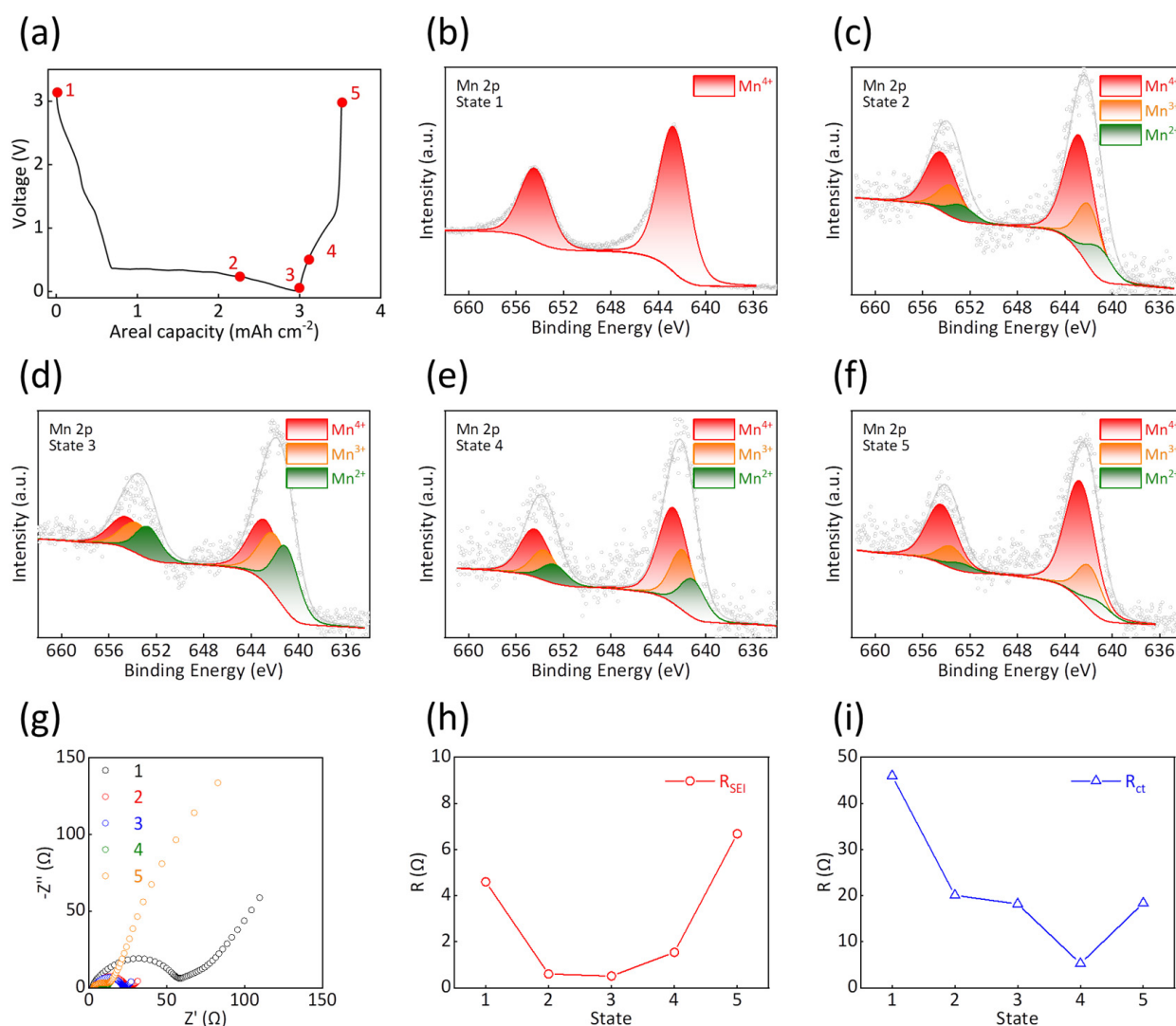
Figure 3. (**a**) Voltage profile of lithiation/delithiation of α-MnO$_2$@CP. These discharge/charge processes were performed within a Li||α-MnO$_2$@CP half cell using liquid electrolyte. The numbers 1–5 depicted in Figure 3a signify various discharge/charge states of the cell, corresponding to different lithiation/delithiation states of α-MnO$_2$@CP, which were subjected to further investigation through XPS and EIS characterizations. (**b**–**f**) Mn 2p XPS spectra of α-MnO$_2$@CP at different states during lithiation/delithiation processes. (**g**) Nyquist plot, (**h**) R_{SEI}, and (**i**) R_{ct} evolution of α-MnO$_2$@CP at different states during lithiation/delithiation processes.

To correlate the lithiation state of the α-MnO$_2$ shell with the Li$^+$ transfer kinetics, EIS measurements of the Li||α-MnO$_2$@CP half cell were recorded at different states during the lithiation/delithiation processes (Figure 3g). By further fitting the EIS spectra, different characteristic impedances, including the ohm impedance related to the bulk conductivity of electrolyte (R_{ohm}), the SEI impedance related to Li$^+$ migration ability through the electrolyte interface (R_{SEI}), and the charge transfer impedance related to Li$^+$ and e$^-$ transfers involved in electrochemical reactions (R_{ct}), were systematically obtained [26]. As shown in Figure S6, the lithiation/delithiation processes performed during a single cycle have no impact on the R_{ohm} value, indicating negligible electrolyte consumption as well as side product accumulation on the electrode surface. Hence, a change in the interfacial impedances, such as R_{SEI} and R_{ct}, should arise from the inherent Li$^+$ transfer properties in α-MnO$_2$@CP. According to the evolution of R_{SEI} (Figure 3h), the Li$^+$ transfer dynamic across the SEI layer increases with lithiation degree, and the lowest R_{SEI} was achieved at state 3, which

corresponds to the fully lithiated state at 0 V. It is noteworthy that no SEI layer should be present at a pristine state (state 1), but the R_{SEI} value of α-MnO$_2$@CP is not very high at this state. The latter issue should be due to the native ability of Li$^+$ adsorption and migration in the α-MnO$_2$ shell, which can act as an artificial "SEI" layer. Otherwise, the value of R_{ct} at state 1 is significantly higher than those of other states (Figure 3i), probably due to the low electronic conductivity of the pristine α-MnO$_2$ shell, while an increase in electronic conductivity of the α-MnO$_2$ shell was probably achieved upon lithiation [27]. Hence, this study on the relationship between lithiation state and interfacial transfer kinetics revealed the importance of a deeply lithiated state of α-MnO$_2$@CP for its application in ASSLMBs, since both high Li$^+$ transportation and charge transfer kinetics can be achieved at this state. Fortunately, when α-MnO$_2$@CP is used as the interlayer between Li and SE, its working potential window is close to that of Li plating/stripping, and thus, it remains in a lithiated state without being fully delithiated.

Based on the improved Li$^+$ transfer kinetics, the ability of α-MnO$_2$@CP to guide uniform Li deposition was further studied. As a control, the morphology of CP at different Li plating states was recorded by SEM and EDS. As shown in Figure 4a, after lithiating to 0 V, the CP fiber was surrounded by a passivation layer compared with its pristine state (Figure S1), but a clear surface still remained. After the further plating of 1 mAh cm^{-2} Li on the lithiated CP matrix, uneven Li deposits were clearly observed on the CP fiber (Figure 4b), indicating that the unmatched Li$^+$/e$^-$ transfer velocities resulted in Li deposition on the e$^-$-enriched zones. With increasing Li plating capacity to 2 mAh cm^{-2}, the heterogeneity of Li deposits was further aggravated, leading to large Li protuberances on the fiber (Figure 4c), which will seriously affect the structural stability at the Li/SE interface. In contrast, for α-MnO$_2$@CP, the fibrous α-MnO$_2$ shell at the pristine state (Figure 1c) was tailored into a tightly interconnected structure after lithiating to 0 V (Figure 4d), which can provide a better fluency of Li$^+$ transportation paths with a high Li$^+$ diffusivity. By further plating 1 mAh cm^{-2} Li, a smooth Li layer was uniformly formed on the α-MnO$_2$@CP fiber (Figure 4e), demonstrating a balanced Li$^+$/e$^-$ transfer across the entire scaffold due to the accelerated Li$^+$ migration in the α-MnO$_2$ shell. The uniform Li deposition feature on α-MnO$_2$@CP was also retained at a higher Li plating capacity of 2 mAh cm^{-2} (Figure 4f), reflecting its ability to ensure a stable Li/SE interface for practical conditions.
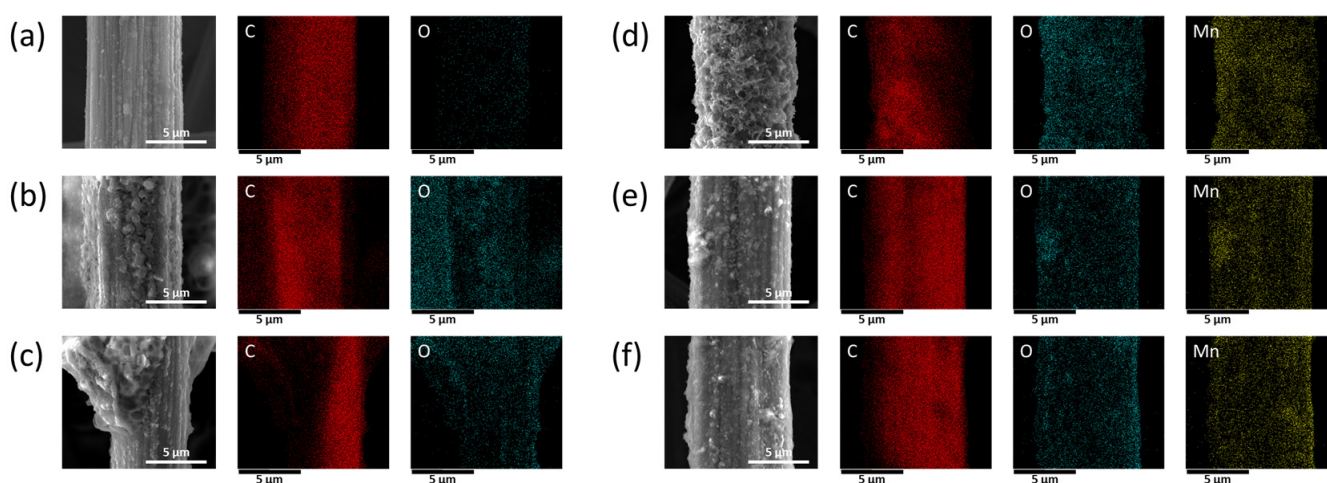

Figure 4. SEM and EDS images of CP fiber (**a**) lithiated to 0 V and after plating (**b**) 1 and (**c**) 2 mAh cm^{-2} Li. SEM and EDS images of α-MnO$_2$@CP fiber (**d**) lithiated to 0 V and after plating (**e**) 1 and (**f**) 2 mAh cm^{-2} Li.

The morphological evolution of the investigated scaffolds was further observed at a larger scale of observation using an optical microscope. As shown in Figure 5a, a golden appearance was observed for the lithiated CP at 0 V due to the formation of Li$_x$C$_6$ [28]. As Li plating proceeded, uneven Li deposition was clearly observed on the lithiated CP matrix,

which is a direct indicator of the unmatched Li^+/e^- transfer velocities, since the fast e^- release to the matrix surface can reduce Li^+ and result in the top Li deposition, inhibiting the Li deposition inside the pores of CP and seriously weakening its Li-hosting ability (as schematically illustrated in Figure 5a). For α-MnO$_2$@CP, no metallic luster deposits were observed at 1 mAh cm^{-2} (Figure 5b), indicating inner Li deposition in the scaffold space, and the very thin Li layer uniformly surrounding the α-MnO$_2$@CP fibers could also be a reason. Despite an observation of some Li deposits at 2 mAh cm^{-2}, the global morphology of α-MnO$_2$@CP was not changed significantly, demonstrating the great ability of α-MnO$_2$@CP to guide uniform Li deposition along the three-dimensional network, as schematically illustrated in Figure 5b.

Figure 5. Optical observation and schematic presentation of morphology change upon Li plating of (**a**) CP and (**b**) α-MnO$_2$@CP. The scale bar is 100 μm.

Finally, the cycling performances of ASSLMBs were assessed at different charge/discharge rates. It should be noted that, during the pre-cycling of ASSLMBs at 0.1C/0.1C ($\sim$0.022 mA cm^{-2}/0.022 mA cm^{-2}), the initial CEs were 93.7%, 93.1%, and 91.3% for the cells using bare Li without an interlayer, the CP interlayer, and the α-MnO$_2$@CP interlayer, respectively (Figure S7). These results show that the use of the α-MnO$_2$@CP interlayer did not significantly decrease the initial CE of the ASSLMBs, and thus, this protective structure is expected for a potential application in practical ASSLMBs. For the charge/discharge rates of 3C/3C ($\sim$0.66 mA cm^{-2}/0.66 mA cm^{-2}), the cell using α-MnO$_2$@CP as the interlayer between Li and SE exhibited stable cycling with a high average coulombic efficiency (CE) of 99.96% and a capacity retention of 71.85% over 4000 cycles (Figure 6a). In contrast, both the cells using bare Li without an interlayer and using the CP interlayer quickly failed in less than 250 cycles. At high charge/discharge rates of 10C/10C ($\sim$2.2 mA cm^{-2}/2.2 mA cm^{-2}), the cells using bare Li without an interlayer and using the CP interlayer quickly failed after the start of cycling, while the cell using α-MnO$_2$@CP still achieved a stable cycling over 7000 cycles, with an average CE of 99.96% and a capacity retention of 61.33% (Figure 6b). This outstanding high-rate cycling performance further demonstrates the fast Li$^+$ transfer at the Li/SE interface enabled by α-MnO$_2$@CP.
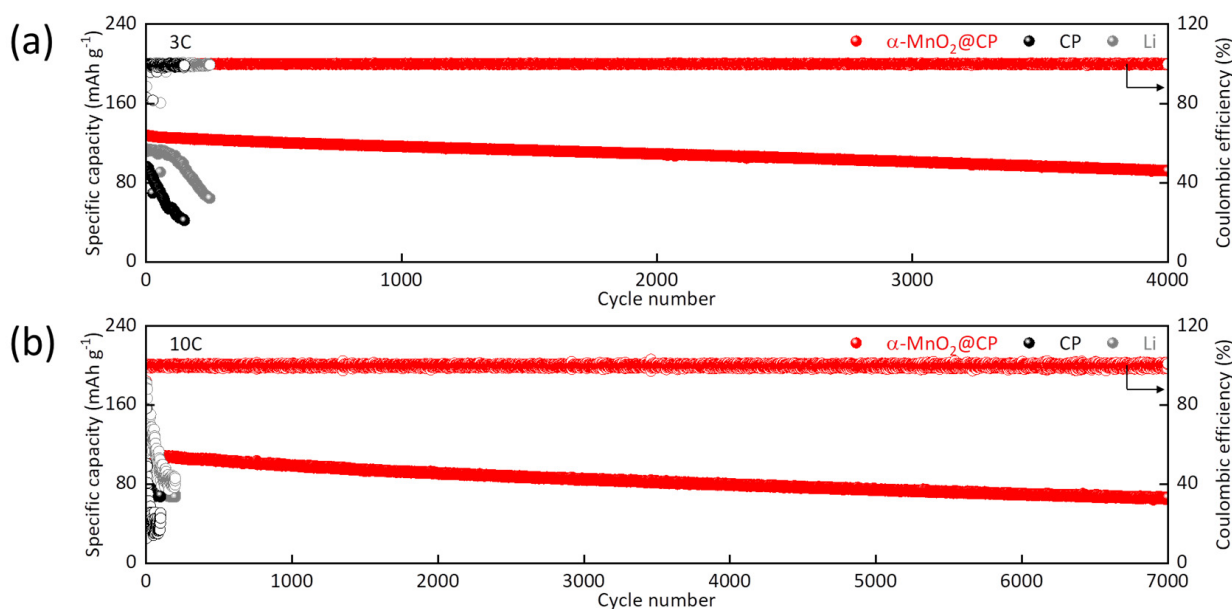

Figure 6. ASSLMB cycling performances at charge/discharge rates of (**a**) 3C/3C and (**b**) 10C/10C.

4. Conclusions

In this work, the α-MnO$_2$-decorated carbon paper (CP) structure (α-MnO$_2$@CP) was proposed to address the sluggish Li$^+$ transfer kinetics at the Li/SE interface of the ASSLMBs. Thanks to the large tunnel structure of the α-MnO$_2$ shell, efficient Li$^+$ adsorption and fast Li$^+$ transportation can be simultaneously enabled across the whole structure of α-MnO$_2$@CP, leading to a high CCD of 3.95 mA cm^{-2} at the Li/SE interface. The outstanding Li$^+$ transfer kinetics also endowed α-MnO$_2$@CP with the ability to guide uniform Li deposition along the scaffold fibers, resulting in a dendrite-suppressed Li/SE interface. Using α-MnO$_2$@CP as the Li/SE interface stabilizer, stable cycling over 7000 cycles at high charge/discharge rates of 10C/10C was achieved for ASSLMBs. This work provides a potential battery designing route to overcome the restrained power density of the next ASSLMBs.

profile of CCD measurement for all-solid-state Li‖Li symmetrical cells using (a) bare Li without interlayer and (b) CP interlayer between Li and SE; Figure S6: R_{ohm} evolution of α-MnO$_2$@CP at different states during lithiation/delithiation processes; Figure S7: Pre-cycling charge/discharge curves of ASSLMBs at 0.1C/0.1C; Table S1: Survey of CCD obtained in recent studies.

Data Availability Statement: The data presented in this study are available on request from the corresponding author on reasonable request.

Conflicts of Interest: The authors declare no conflict of interest.

References

1. Cano, Z.P.; Banham, D.; Ye, S.Y.; Hintennach, A.; Lu, J.; Fowler, M.; Chen, Z.W. Batteries and fuel cells for emerging electric vehicle markets. *Nat. Energy* **2018**, *3*, 279–289. [CrossRef]
2. Wang, F.F.; Ke, X.Y.; Shen, K.; Zhu, L.; Yuan, C. A Critical Review on Materials and Fabrications of Thermally Stable Separators for Lithium-Ion Batteries. *Adv. Mater. Technol.* **2022**, *7*, 2100772. [CrossRef]
3. Placke, T.; Kloepsch, R.; Dühnen, S.; Winter, M. Lithium ion, lithium metal, and alternative rechargeable battery technologies: The odyssey for high energy density. *J. Solid State Electrochem.* **2017**, *21*, 1939–1964. [CrossRef]
4. Chu, S.; Majumdar, A. Opportunities and challenges for a sustainable energy future. *Nature* **2012**, *488*, 294–303. [CrossRef] [PubMed]
5. Xu, K. Nonaqueous liquid electrolytes for lithium-based rechargeable batteries. *Chem. Rev.* **2004**, *104*, 4303–4417. [CrossRef] [PubMed]
6. Manthiram, A.; Yu, X.W.; Wang, S.F. Lithium battery chemistries enabled by solid-state electrolytes. *Nat. Rev. Mater.* **2017**, *2*, 16103. [CrossRef]
7. Peljo, P.; Girault, H.H. Electrochemical potential window of battery electrolytes: The HOMO-LUMO misconception. *Energy Environ. Sci.* **2018**, *11*, 2306–2309. [CrossRef]
8. Wang, C.H.; Adair, K.R.; Liang, J.W.; Li, X.N.; Sun, Y.P.; Li, X.; Wang, J.W.; Sun, Q.; Zhao, F.P.; Lin, X.T.; et al. Solid-State Plastic Crystal Electrolytes: Effective Protection Interlayers for Sulfide-Based All-Solid-State Lithium Metal Batteries. *Adv. Funct. Mater.* **2019**, *29*, 1900392. [CrossRef]
9. Park, H.; Kim, J.; Lee, D.; Park, J.; Jo, S.; Kim, J.; Song, T.; Paik, U. Epitaxial Growth of Nanostructured Li2Se on Lithium Metal for All Solid-State Batteries. *Adv. Sci.* **2021**, *8*, 2004204. [CrossRef]
10. Chen, Y.; Li, W.W.; Sun, C.Z.; Jin, J.; Wang, Q.; Chen, X.D.; Zha, W.P.; Wen, Z.Y. Sustained Release-Driven Formation of Ultrastable SEI between Li$_6$PS$_5$Cl and Lithium Anode for Sulfide-Based Solid-State Batteries. *Adv. Energy Mater.* **2021**, *11*, 2002545. [CrossRef]
11. Cao, Y.; Zuo, P.J.; Lou, S.F.; Sun, Z.; Li, Q.; Huo, H.; Ma, Y.L.; Du, C.Y.; Gao, Y.Z.; Yin, G.P. A quasi-solid-state Li-S battery with high energy density, superior stability and safety. *J. Mater. Chem. A* **2019**, *7*, 6533–6542. [CrossRef]
12. Wan, H.; Liu, S.; Deng, T.; Xu, J.; Zhang, J.; He, X.; Ji, X.; Yao, X.; Wang, C. Bifunctional Interphase-Enabled Li$_{10}$GeP$_2$S$_{12}$ Electrolytes for Lithium−Sulfur Battery. *ACS Energy Lett.* **2021**, *6*, 862–868. [CrossRef]
13. Chang, X.; Liu, G.; Wu, M.; Chang, M.; Zhao, X.; Chen, G.Z.; Fow, K.L.; Yao, X. Dual-functional ZnO/LiF layer protected lithium metal for stable Li$_{10}$GeP$_2$S$_{12}$-based all-solid-state lithium batteries. *Battery Energy* **2023**, *2*, 20220051. [CrossRef]
14. Chen, Z.; Liang, Z.; Zhong, H.; Su, Y.; Wang, K.; Yang, Y. Bulk/Interfacial Synergetic Approaches Enable the Stable Anode for High Energy Density All-Solid-State Lithium−Sulfur Batteries. *ACS Energy Lett.* **2022**, *7*, 2761–2770. [CrossRef]
15. Lee, S.; Lee, K.; Kim, S.; Yoon, K.; Han, S.; Lee, M.H.; Ko, Y.; Noh, J.H.; Kim, W.; Kang, K. Design of a lithiophilic and electron-blocking interlayer for dendrite-free lithium-metal solid-state batteries. *Sci. Adv.* **2022**, *8*, eabq0153. [CrossRef] [PubMed]
16. Sung, J.; Kim, S.Y.; Harutyunyan, A.; Amirmaleki, M.; Lee, Y.; Son, Y.; Li, J. Ultra-Thin Lithium Silicide Interlayer for Solid-State Lithium-Metal Batteries. *Adv. Mater.* **2023**, *35*, 2210835. [CrossRef] [PubMed]
17. Ling, C.; Mizuno, F. Capture Lithium in αMnO$_2$: Insights from First Principles. *Chem. Mater.* **2012**, *24*, 3943–3951. [CrossRef]
18. Liu, B.; Sun, Y.; Liu, L.; Xu, S.; Yan, X. Advances in Manganese-Based Oxides Cathodic Electrocatalysts for Li–Air Batteries. *Adv. Funct. Mater.* **2018**, *28*, 1704973. [CrossRef]
19. Zhu, G.; Zhu, W.; Lou, Y.; Ma, J.; Yao, W.; Zong, R.; Zhu, Y. Encapsulate α-MnO2 nanofiber within graphene layer to tune surface electronic structure for efficient ozone decomposition. *Nat. Commun.* **2021**, *12*, 4152. [CrossRef]

20. Zhang, R.; Yu, X.; Nam, K.-W.; Ling, C.; Arthur, T.S.; Song, W.; Knapp, A.M.; Ehrlich, S.N.; Yang, X.-Q.; Matsui, M. α-MnO$_2$ as a cathode material for rechargeable Mg batteries. *Electrochem. Commun.* **2012**, *23*, 110–113. [CrossRef]
21. Johnson, C.S. Development and utility of manganese oxides as cathodes in lithium batteries. *J. Power Sources* **2007**, *165*, 559–565. [CrossRef]
22. Zhang, H.; Cao, G.; Wang, Z.; Yang, Y.; Shi, Z.; Gu, Z. Growth of Manganese Oxide Nanoflowers on Vertically-Aligned Carbon Nanotube Arrays for High-Rate Electrochemical Capacitive Energy Storage. *Nano Lett.* **2008**, *8*, 2664–2668. [CrossRef] [PubMed]
23. Débart, A.; Paterson, A.J.; Bao, J.; Bruce, P.G. α-MnO$_2$ Nanowires: A Catalyst for the O$_2$ Electrode in Rechargeable Lithium Batteries. *Angew. Chem. Int. Ed.* **2008**, *47*, 4521–4524. [CrossRef] [PubMed]
24. Li, Q.; Zhu, S.; Lu, Y. 3D Porous Cu Current Collector/Li-Metal Composite Anode for Stable Lithium-Metal Batteries. *Adv. Funct. Mater.* **2017**, *27*, 1606422. [CrossRef]
25. Zuo, T.-T.; Wu, X.-W.; Yang, C.-P.; Yin, Y.-X.; Ye, H.; Li, N.-W.; Guo, Y.-G. Graphitized Carbon Fibers as Multifunctional 3D Current Collectors for High Areal Capacity Li Anodes. *Adv. Mater.* **2017**, *29*, 1700389. [CrossRef] [PubMed]
26. Zhao, Z.; Zou, Y.; Liu, P.; Lai, Z.; Wen, L.; Jin, Y. EIS equivalent circuit model prediction using interpretable machine learning and parameter identification using global optimization algorithms. *Electrochim. Acta* **2022**, *418*, 140350. [CrossRef]
27. Le, M.; Liu, Y.; Wang, H.; Dutta, R.K.; Yan, W.; Hemminger, J.C.; Wu, R.Q.; Penner, R.M. In Situ Electrical Conductivity of Li$_x$MnO$_2$ Nanowires as a Function of x and Size. *Chem. Mater.* **2015**, *27*, 3494–3504. [CrossRef]
28. Duan, J.; Zheng, Y.; Luo, W.; Wu, W.; Wang, T.; Xie, Y.; Li, S.; Li, J.; Huang, Y. Is graphite lithiophobic or lithiophilic? Natl. *Sci. Rev.* **2020**, *7*, 1208.